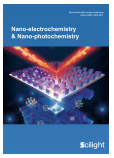
Nano-electrochemistry & Nano-photochemistry
https://www.sciltp.com/journals/nenp



Article

Check for updates

Theoretical Insights into Electrocatalytic CO_2 Reduction to C_2H_4 via Bridging-Mode Asymmetric Coupling over Bimetallic Triatomic Clusters

Shilin Wei, Hongguang Wang, Peiyao Bai and Lang Xu *

Jiangsu Key Laboratory for Clean Utilization of Carbon Resources, School of Chemical Engineering and Technology, China University of Mining and Technology, Xuzhou 221116, China
* Correspondence: lang.xu@cumt.edu.cn

How To Cite: Wei, S.; Wang, H.; Bai, P.; et al. Theoretical Insights into Electrocatalytic CO_2 Reduction to C_2H_4 via Bridging-Mode Asymmetric Coupling over Bimetallic Triatomic Clusters. *Nano-electrochemistry & Nano-photochemistry* **2026**, *2*(4), 23. https://doi.org/10.53941/nenp.2026.100023

Received: 16 August 2026
Revised: 17 September 2026
Accepted: 8 October 2026
Published: 19 October 2026

Abstract: Bridging-mode asymmetric coupling of *CHO and *CO governs C_2H_4 selectivity over Cu_2TM/β-TBN bimetallic triatomic clusters for electrocatalytic CO_2 reduction. In these catalysts, two Cu atoms and a transition metal (TM = Ti ~ Zn, Zr ~ Cd) dopant are anchored on a β-phase tetragonal borophene nanosheet. After screening fourth- and fifth-period TM dopants for thermodynamic stability and CO_2 activation, twelve systems were examined. CO_2 adsorbs preferentially in a bridging geometry at the Cu(1)–TM site, its adsorption energy scaling linearly with the TM d-band center. Of the three possible C–C coupling routes, the most favorable is the asymmetric coupling of bridge-adsorbed *CHO with adjacent *CO, yielding *CHOCO[1,2,3], in which the three metal sites jointly coordinate the oxygen and carbon atoms. This route, enabled by the simultaneous engagement of all three metal sites, is inaccessible on single-site or dual-site catalysts. Thermodynamic stability alone proves an insufficient guide. The formation free energy of the *CHO+*CO precursor, ΔG(*CHO+*CO), and the C–C coupling transition-state energy barrier, E_{TS}, are inversely correlated. Excess stabilization of the intermediate raises the kinetic barrier, overstabilizing the precursor in a manner that hinders the coupling step rather than promoting it. This thermodynamic-kinetic trade-off demands a balanced intermediate affinity. Resolving this trade-off reveals a period-dependent divergence in regulatory mechanism. For fourth-period TMs, electron transfer between adsorbate and surface predominates, with geometric displacement playing a secondary role. For fifth-period TMs, vertical displacement of the TM atom dominates, as confirmed by cross-correlation analysis. Electronic and geometric controls, distinct in origin yet convergent in function, define a unified design space for C–C coupling catalysts.

Keywords: electrocatalytic CO_2 reduction; bimetallic triatomic clusters; bridging-mode asymmetric coupling; C–C coupling; borophene; electronic and geometric modulation

1. Introduction

Rising CO_2 emissions have disrupted the natural carbon cycle, driving profound climate and environmental change [1,2]. Converting CO_2 into valuable chemical products using renewable electricity represents a strategy that reaches beyond emission mitigation, aiming instead to restore the carbon cycle itself [3–5]. The electrocatalytic CO_2 reduction reaction (CO_2RR) offers a promising route to high-value-added chemicals such as

Copyright: © 2026 by the authors. This is an open access article under the terms and conditions of the Creative Commons Attribution (CC BY) license (https://creativecommons.org/licenses/by/4.0/).
Publisher's Note: Scilight stays neutral with regard to jurisdictional claims in published maps and institutional affiliations.

C_2H_4 under mild conditions [6,7]. However, the efficient and selective synthesis of C_2H_4 remains a formidable challenge [8–10]. The central bottleneck lies not in the initial activation of CO_2, but in the C–C coupling step, where an intricate mechanism and a persistently high kinetic barrier constrain both product selectivity and overall yield [11]. Advancing C_2H_4 production therefore demands catalyst platforms that can host multiple C–C coupling pathways and discriminate among them, enabling the key intermediates and their specific interactions with surface sites to be resolved and then rationally tuned [12–14]. This imperative has motivated the search for catalysts beyond the single-site design, where multisite architectures supply the cooperative binding environments essential for steering selective C–C bond formation.

Single-atom catalysts (SACs), with their structurally uniform and well-defined active sites, have served as powerful computational and experimental platforms for resolving structure-activity relationships in electrocatalysis [15–19]. However, the very attribute that enables this resolving power, the spatial isolation of the active metal center, also imposes a fundamental constraint on CO_2RR product scope. A single metal site cannot simultaneously accommodate two carbon-based intermediates in the proximity and orientation required for concerted C–C coupling, a prerequisite for forming C_2H_4 [20]. This intrinsic limitation has motivated a progressive expansion of the catalytic architecture from one to two and then to three adjacent metal centers. Dual-atom catalysts (DACs) introduced a second site, and triatomic catalysts (TACs) extend the design to a triangular three-center geometry [21,22]. It is this triangular configuration that qualitatively distinguishes TACs from both SACs and DACs. Three metal atoms arranged in spatial proximity generate a diverse set of adsorption microenvironments, enabling binding modes such as bridging configurations and asymmetric dual-site anchoring that are structurally inaccessible on single atoms or atom pairs. This expanded configurational space offers systematic control over the stability and coupling geometry of key intermediates, positioning TACs as a uniquely suitable platform for investigating and optimizing C–C coupling pathways toward C_2H_4 production [23].

The rational design of a triatomic cluster for CO_2RR rests on the selection of three components, each assigned a distinct catalytic function: a primary metal that supplies the intrinsic activity for C–C coupling, a dopant that modulates the electronic environment, and a substrate that enforces the correct atomic geometry. Copper serves as the natural choice for the primary metal. Its intermediate *CO binding strength, sufficient to retain the adsorbate for coupling without inducing surface poisoning, distinguishes Cu as the most effective monometallic electrocatalyst for C–C bond formation in CO_2RR [24]. Building on this intrinsic activity of Cu, a transition metal (TM) atom is introduced to replace one Cu, converting the homonuclear Cu–Cu pair into a heteronuclear Cu–TM pair within the trimer. This substitution breaks the local electronic symmetry, generating chemically inequivalent binding sites across the three metal centers. As a result, the cluster can simultaneously accommodate distinct carbon intermediates, specifically *CO on one type of site and *CHO on another, in the relative orientation that selective C–C coupling demands. To realize this trimer geometry with atomic precision, the substrate must present a periodic array of structurally defined anchoring pockets. Two-dimensional borophene nanosheets, and in particular the β-phase tetragonal borophene (β-TBN), satisfy this structural requirement [25–30]. β-TBN features extended linear chains of boron vacancies, continuous rows of electron-deficient cavities that can seat two Cu atoms and a heterometal atom in adjacent positions, thereby enforcing the triangular arrangement that underpins multisite cooperativity [31].

This work addresses a central question in the design of triatomic CO_2RR catalysts. Given a Cu_2TM trimer anchored on β-TBN, which C–C coupling pathway operates, what governs the stability of the coupling precursor, and how electronic and geometric factors separately contribute to tuning that stability across the transition metal series. To answer these questions, twelve Cu_2TM/β-TBN catalysts (TM = Ti, V, Cr, Mn, Fe, Cu, Zr, Nb, Mo, Tc, Ru, Pd) were systematically investigated using density functional theory, after excluding TM dopants that do not satisfy the thermodynamic stability or CO_2 activation criteria. The three metal sites, labeled Cu(1), Cu(2), and TM, form a triangular architecture that enables multiple binding modes for carbonaceous intermediates. Three distinct C–C coupling pathways were evaluated, and the thermodynamically dominant route was identified. The formation free energy of the *CHO+*CO precursor, ΔG(*CHO+*CO), was found to correlate inversely with the C–C coupling transition-state energy barrier, E_{TS}, revealing a thermodynamic-kinetic trade-off that defines an optimal window of intermediate affinity. The regulatory mechanism governing ΔG(*CHO+*CO) was further resolved into two period-dependent modes. For fourth-period TMs, electron transfer between the adsorbate and the cluster serves as the primary controlling factor. For fifth-period TMs, the vertical displacement of the TM atom assumes the dominant role, a geometric descriptor substantially decoupled from charge transfer effects. These findings establish electronic charge transfer and vertical displacement of the TM atom as complementary and predictive descriptors for C–C coupling activity, offering a dual-descriptor strategy for the rational screening and design of triatomic CO_2RR catalysts.

2. Computational Details

All density functional theory calculations were performed using the Vienna Ab initio Simulation Package (VASP) [32–34]. The projector-augmented wave (PAW) method described the electron-ion interactions [35,36], and the Perdew-Burke-Ernzerhof (PBE) functional within the generalized gradient approximation (GGA) treated exchange and correlation [37,38]. A plane-wave cutoff of 450 eV was employed, and structural relaxations were converged to 10^{-5} eV in total energy and 0.02 eV Å^{-1} in atomic forces. The Brillouin zone was sampled with a 4 × 4 × 1 Gamma-centered k-point mesh [39]. A vacuum region of 15 Å along the z-direction separated periodic images of the borophene sheet. Long-range van der Waals interactions were included through Grimme's DFT-D3 dispersion correction [40]. Identical computational parameters were applied to all Cu_2TM/β-TBN systems to ensure consistent comparison across the TM series.

Reaction free energies were evaluated within the computational hydrogen electrode (CHE) framework [41], in which the free energy of a proton-electron pair ($H^+ + e^-$) is referenced to that of $0.5H_2$ at $U = 0$ V versus the reversible hydrogen electrode. The free energy change for each elementary step was computed as

$$\Delta G = \Delta E_{DFT} + \Delta E_{ZPE} + \int C_p \, dT - T\Delta S$$

where ΔE_{DFT} denotes the DFT energy difference, ΔE_{ZPE} the zero-point energy contribution, C_p the heat capacity, ΔS the entropy change, and T the absolute temperature.

The binding energy E_b of a Cu_2TM/β-TBN system relative to its constituent fragments was calculated as

$$E_b = E_{Cu2TM/\beta\text{-}TBN} - E_{\beta\text{-}TBN} - 2E_{Cu} - E_{TM}$$

where $E_{Cu2TM/\beta\text{-}TBN}$, $E_{\beta\text{-}TBN}$, E_{Cu}, and E_{TM} denote the total energies of the catalyst-substrate complex, the pristine β-TBN sheet, an isolated Cu atom, and an isolated TM atom, respectively.

The d-band center ε_d was evaluated from the density of d states $n_d(\varepsilon)$ as

$$\varepsilon_d = (\int n_d(\varepsilon)\varepsilon d\varepsilon)/(\int n_d(\varepsilon)d\varepsilon)$$

where $\int n_d(\varepsilon)d\varepsilon$ represents the integral of the density of states of the d orbitals of Cu_2TM/β-TBN, and $\int n_d(\varepsilon)\varepsilon d\varepsilon$ represents the integral of the product of the density of states and the corresponding energy level.

Crystal orbital Hamilton population (COHP) analysis was carried out with the LOBSTER program to probe chemical bonding in adsorbed CO_2 and in the C–C coupling precursor *CHO+*CO [42–45]. Bond strengths were quantified by the integrated COHP (ICOHP) values of C–O and TM–O bonds, where more negative ICOHP indicates stronger bonding. Transition-state energy barriers for C–C coupling were located using the climbing image nudged elastic band (CINEB) method [46]. Zero-point energy corrections were included in these transition-state calculations.

3. Results and Discussion

3.1. Geometric and Electronic Structure of Cu_2TM/β-TBN

A series of eighteen Cu_2TM/β-TBN triatomic clusters, spanning the fourth-period and fifth-period transition metals (TM = Ti, V, Cr, Mn, Fe, Co, Ni, Cu, Zn, Zr, Nb, Mo, Tc, Ru, Rh, Pd, Ag, Cd), were constructed by anchoring two Cu atoms and one TM atom onto the linear vacancy chains of β-TBN. In each structure, the three metal atoms adopt a triangular geometry, with the two Cu atoms occupying adjacent vacancies on the same chain and the TM atom positioned at the neighboring vacancy site (Figure 1a). The two Cu sites are labeled Cu(1) and Cu(2), and the heterometal site is denoted as TM.

To characterize the geometric features of these clusters, four structural parameters were computed, the interatomic distances $d_{Cu(1)–Cu(2)}$, $d_{Cu(1)–TM}$, and $d_{Cu(2)–TM}$, and the vertical displacement of the TM atom from the β-TBN plane, $d_{TM–\beta\text{-}TBN}$ (Figure 1a and Table S1). Normalizing the three interatomic distances and projecting them onto a ternary diagram (Figure 1b) provides a compact visual representation of the pairwise distance relationships. A clear structural regularity emerges. For sixteen of the eighteen clusters, $d_{Cu(1)–TM}$ and $d_{Cu(2)–TM}$ are essentially equal, and the data points align along a single straight line. The only exceptions are Cu_2Ni/β-TBN and Cu_2Tc/β-TBN, where the two Cu–TM distances differ. There, the broken symmetry arises from the anisotropic d-orbital interaction between the TM atom and the two Cu sites. Ni and Tc possess partially filled d orbitals, whose coupling to the asymmetric boron-vacancy environment of β-TBN differs between the two Cu neighbors. This inequivalent orbital overlap induces a local Jahn-Teller-like distortion, which shortens one Cu–TM bond and lengthens the other. This near-degeneracy of $d_{Cu(1)–TM}$ and $d_{Cu(2)–TM}$ across the majority of systems reveals that Cu(1) and Cu(2)

are symmetrically positioned with respect to the TM site. The structural symmetry implies that Cu(1) and Cu(2) reside in similar local electronic environments, an expectation confirmed by their electron localization functions (ELF), as shown in Figure S1. The ELF maps confirm that, for all systems except Cu_2Ni/β-TBN and Cu_2Tc/β-TBN, the spatial distribution of electron density surrounding Cu(1) and Cu(2) is highly symmetric with respect to the TM atom. This electronic symmetry is consistent with the geometric equivalence established by the interatomic distances (Table S1). In contrast to the lateral Cu–TM symmetry, the vertical displacement $d_{TM–β-TBN}$ varies widely across the series (Figure S2 and Table S1). The TM atom ranges from being nearly coplanar with the Cu pair to protruding prominently above it. This vertical displacement generates local dipole moments and asymmetric charge distributions that provide a geometric mechanism for modulating the electronic structure and the d-band center of the cluster.

Thermodynamic stability provides the first screening criterion. The binding energies of the eighteen Cu_2TM/β-TBN structures were displayed in Figure 1c. Cu_2Zn/β-TBN and Cu_2Cd/β-TBN exhibit positive binding energies of 0.10 eV and 0.71 eV, respectively, indicating that they are unstable against decomposition. All remaining sixteen structures possess negative binding energies, confirming their thermodynamic stability. Cu_2Zn/β-TBN and Cu_2Cd/β-TBN are therefore excluded from subsequent analysis, reducing the candidate pool to sixteen systems.

The electronic structure of the Cu_2TM/β-TBN series was characterized through the d-band centers of the overall cluster, $\varepsilon_d(Cu_2TM)$, and of the individual metal atoms, $\varepsilon_d(Cu)$ and $\varepsilon_d(TM)$ (Figure S3). Across the fixed β-TBN substrate, $\varepsilon_d(Cu_2TM)$ scales linearly with $\varepsilon_d(TM)$ (Figure 1d). As the $\varepsilon_d(TM)$ shifts to lower energy, $\varepsilon_d(Cu_2TM)$ follows this downward trend in a correlated manner. The Cu d-band center, by contrast, exhibits no systematic dependence on $\varepsilon_d(Cu_2TM)$ (Figure S4). The TM atom therefore serves as the primary electronic modulator. Its d states dominate the electronic structure near the Fermi level, and substituting the TM identity predictably shifts the global d-band center of the cluster.

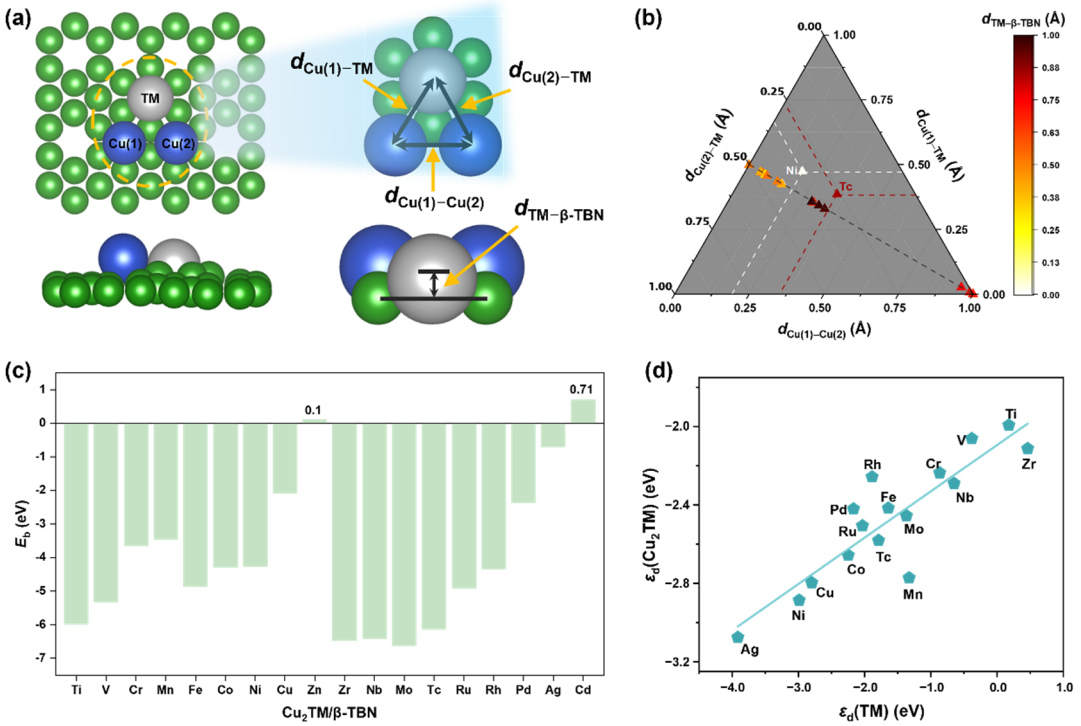


Figure 1. Structural and electronic characterization of Cu_2TM/β-TBN triatomic clusters. (**a**) Schematic of the Cu_2TM/β-TBN structure, showing the triangular arrangement of the three metal sites. Cu(1) and Cu(2) denote the two Cu sites, and TM denotes the transition metal dopant site. (**b**) Ternary diagram constructed from the normalized interatomic distances $d_{Cu(1)–Cu(2)}$, $d_{Cu(1)–TM}$, and $d_{Cu(2)–TM}$. (**c**) Binding energy for the eighteen Cu_2TM/β-TBN systems. (**d**) Linear correlation between $\varepsilon_d(Cu_2TM)$ and $\varepsilon_d(TM)$.

3.2. CO_2 Adsorption and Activation

The triangular Cu_2TM architecture presents three distinct pairs of metal sites capable of accommodating a bridging CO_2 molecule, corresponding to the configurations labeled *CO_2[1,2] (Cu(1)–Cu(2) bridge), *CO_2[2,3] (Cu(2)–TM bridge), and *CO_2[1,3] (Cu(1)–TM bridge) (Figure 2a). The adsorption energies of these three

configurations were evaluated across the Cu_2TM/β-TBN series (Table S2). For every system in which Cu(1) and Cu(2) are electronically equivalent, *CO_2[1,3] and *CO_2[2,3] are energetically degenerate, a direct consequence of the axial symmetry and ELF equivalence documented above (Figure S1 and Table S1). Cu_2Ni/β-TBN and Cu_2Tc/β-TBN, where this electronic symmetry is broken, lift the degeneracy, but even in these two cases *CO_2[1,3] remains the lower-energy configuration relative to *CO_2[2,3] (Table S2). When the *CO_2[1,2] configuration is a stable local minimum on the potential energy surface, *CO_2[1,3] is always the lower-energy state. For Ti, Zr, Nb, and Ru, no such minimum exists, as the *CO_2[1,2] starting geometry relaxes to an alternative binding mode. This energetic ordering, which reflects the stronger oxophilicity of the TM site relative to Cu and is analyzed in detail through COHP bonding analysis in the following section, establishes *CO_2[1,3] as the dominant and universal CO_2 adsorption configuration on Cu_2TM/β-TBN. This bridging configuration across the heterometallic Cu–TM pair establishes the initial state from which all subsequent reduction and C–C coupling steps proceed.

The *CO_2[1,3] adsorption energy exhibits a clear periodic dependence. Within each transition metal period, E_{ads}(*CO_2[1,3]) increases with atomic number (Figure 2b), a trend that points to an electronic origin rooted in the identity of the TM. To assess the extent of CO_2 activation upon adsorption, the internal geometry of the adsorbed CO_2 was examined. The oxygen atom that is not coordinated to any cluster atom is labeled O(1), and that bound to the TM site is labeled O(2). Two structural parameters were monitored, the C–O bond lengths, $d_{C–O(1)}$ and $d_{C–O(2)}$, and the O–C–O bond angle θ (Figure 2c,d). For the majority of Cu_2TM/β-TBN systems, the C–O bonds elongate relative to gas-phase CO_2, and θ deviates significantly from 180°, both signatures of a bent, activated CO_2 molecule. Cu_2Co/β-TBN, Cu_2Ni/β-TBN, and Cu_2Ag/β-TBN depart from this pattern. On these three surfaces, the bond angle θ remains near 180°, and the C–O bond lengths stay close to their gas-phase values (Figure S5). These geometric features identify CO_2 adsorption as physisorption rather than chemisorption. Activation is negligible on these surfaces. Co, Ni, and Ag were therefore excluded from further consideration. This second screening step reduces the candidate pool from sixteen to thirteen systems. One additional system will be eliminated following the C–C coupling analysis.

With the inactive dopants removed, the electronic driver of CO_2 adsorption comes into clear view. For the thirteen active systems, E_{ads}(*CO_2[1,3]) scales linearly with the TM d-band center ε_d(TM) (Figure 2e). As ε_d(TM) shifts to lower energy, the CO_2 adsorption strength rises progressively. This linear relationship establishes ε_d(TM) as an effective electronic descriptor for CO_2 binding on Cu_2TM/β-TBN. Across this active series, the geometric parameter $d_{TM–β-TBN}$ varies independently and does not disrupt the correlation, confirming that the d-band center is the primary electronic factor governing CO_2 adsorption strength.

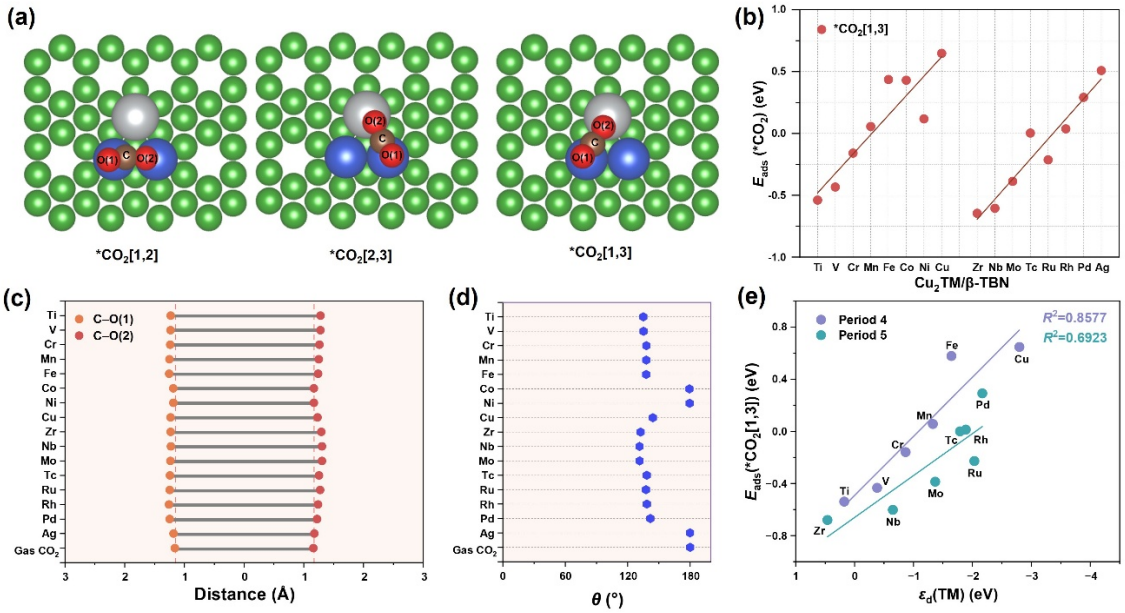


Figure 2. CO_2 adsorption on Cu_2TM/β-TBN. (**a**) Three possible CO_2 adsorption configurations, *CO_2[1,2] (bridging Cu(1) and Cu(2)), *CO_2[2,3] (bridging Cu(2) and TM), and *CO_2[1,3] (bridging Cu(1) and TM). (**b**) Adsorption energies of *CO_2 on Cu_2TM/β-TBN. (**c**) C–O bond lengths, $d_{C–O(1)}$ and $d_{C–O(2)}$ for CO_2 in the *CO_2[1,3] configuration. O(1) and O(2) denote the uncoordinated and TM-bound oxygen atoms, respectively. (**d**) Bond angle θ for the *CO_2[1,3] configuration. (**e**) Linear correlation between E_{ads}(*CO_2[1,3]) and ε_d(TM).

The geometric preference for *CO_2[1,3] adsorption is rooted in the chemical bonding between the activated CO_2 molecule and the catalyst surface. Crystal orbital Hamilton population (COHP) analysis was employed to quantify the C–O bond strengths in the adsorbed state (Figure 3a). The integrated COHP (ICOHP) values of the two inequivalent C–O bonds were examined across the series. ICOHP(C–O(2)), associated with the oxygen coordinated to the TM site, correlates linearly with ε_d(TM) (Figure 3b,c). As ε_d(TM) shifts to lower energy, ICOHP(C–O(2)) becomes progressively more negative, reflecting a steady strengthening of the TM–O interaction and enhanced electron back-donation from the TM into the CO_2 π^* orbitals. The correlation holds for both fourth-period and fifth-period TM dopants. In sharp contrast, ICOHP(C–O(1)) exhibits no systematic dependence on ε_d(TM). This contrasting behavior demonstrates that the electronic influence of the TM is spatially localized to its immediate coordination sphere and does not propagate through the CO_2 molecule to the C–O(1) bond. The TM site therefore serves as the primary site of electronic activation within the Cu–TM bridge, selectively modulating the C–O(2) bond strength through its d-band center. The Cu(1) site, electronically less responsive to the TM identity, provides a structurally essential anchoring point whose local bonding environment remains stable across the catalyst series. This site-specific electronic response is the bonding-level manifestation of the heterometallic synergy that distinguishes the Cu_2TM triatomic architecture.

The final exclusion concerns Cu_2Rh/β-TBN. Its TM–O bond in the *CHO+*CO intermediate is excessively strong (ICOHP = −1.89, Figure S6), binding the precursor too strongly for the subsequent C–C coupling step to proceed, as quantified in the transition-state analysis below. Consequently, the full screening cascade delivers twelve viable Cu_2TM/β-TBN catalysts, six with fourth-period TMs (Ti, V, Cr, Mn, Fe, Cu) and six with fifth-period TMs (Zr, Nb, Mo, Tc, Ru, Pd). These twelve systems are the subject of the C–C coupling kinetic analysis that follows.

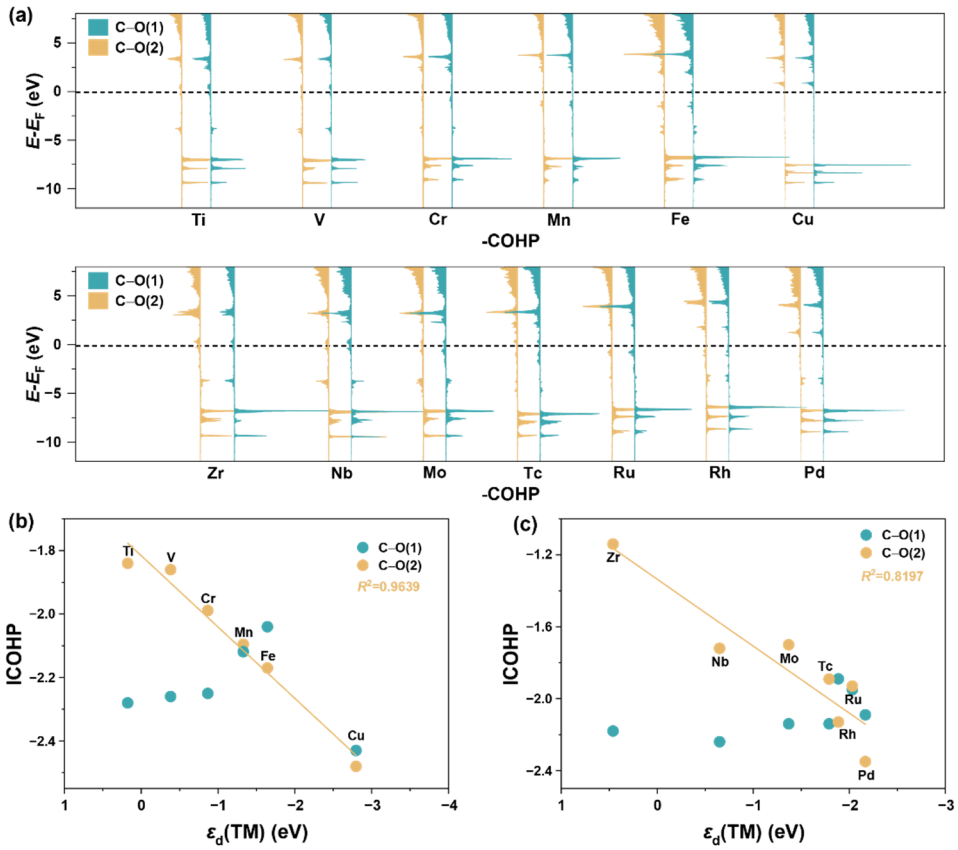


Figure 3. Chemical bonding analysis of CO_2 adsorbed in the *CO_2[1,3] configuration. (a) Crystal orbital Hamilton population (COHP) plots for the C–O bonds in adsorbed *CO_2 on representative Cu_2TM/β-TBN systems. (b) Linear correlation between ICOHP(C–O(2)) and ε_d(TM) for fourth-period TM dopants. (c) Same as (b) but for fifth-period TM dopants.

3.3. C–C Coupling Pathway Selection

Three distinct C–C coupling pathways, differing in the adsorption geometry of the coupling precursors, were identified on the Cu_2TM/β-TBN surface [47,48] (Figure 4a). In pathway I, two *CO species couple directly to form

*OCCO. In pathway II, one *CO undergoes a proton-electron transfer to *CHO, which then couples with an adjacent *CO adsorbed on a single Cu site, yielding *CHOCO[1,2]. Pathway III proceeds through the same initial hydrogenation but with a decisive geometric distinction. The *CHO intermediate adopts a bridging adsorption mode across the Cu(1) and TM sites, and this bridge-adsorbed *CHO subsequently couples with a neighboring *CO adsorbed on Cu(2) to generate the *CHOCO[1,2,3] structure. In this configuration, the TM atom coordinates the oxygen of *CHO, Cu(1) anchors its carbon, and all three metal sites participate in stabilizing the coupling adduct.

The Gibbs free energies of the key intermediates in these three pathways were computed and compared (Figure 4b,c). On every catalyst surface examined, ΔG(*CHO+*CO[1,2,3]) lies below both ΔG(*OCCO) and ΔG(*CHO+*CO[1,2]). This consistent thermodynamic advantage identifies pathway III as the dominant C–C coupling route on Cu_2TM/β-TBN. The structural origin of this preference is the dual-site bridging mode unique to the *CHO+*CO[1,2,3] configuration. The TM–O coordination bond and the Cu(1)–C interaction together restrict the internal rotations of the *CHO moiety, reducing the entropic penalty for bringing the two carbon atoms into coupling proximity. This dual-site anchoring also prepositions the carbon centers with a favorable spatial alignment for C–C bond formation. Pathway I provides no such spatial organization. Two linearly adsorbed *CO species must approach each other without orientational guidance, incurring a substantial kinetic cost. Pathway II introduces *CHO but anchors it linearly on a single Cu site, lacking both the rotational constraint and the spatial preorganization supplied by the TM–Cu bridge. Pathway III is therefore not only thermodynamically favored but uniquely exploits the multisite architecture of the triatomic cluster to steer the C–C coupling event. Thermodynamic favorability alone, however, does not guarantee efficient coupling. As the following section demonstrates, an excessively stabilized *CHO+*CO precursor raises the C–C coupling barrier, introducing a kinetic trade-off that refines the catalyst design principles beyond the thermodynamic screening presented here. The complete free energy profiles for CO_2-to-C_2H_4 conversion via pathway III on all twelve active catalysts are provided in Figures S7–S9. The magnetic moments of the bare clusters and the intermediate states are summarized in Table S3 to rule out spin-state artifacts in the free energies.

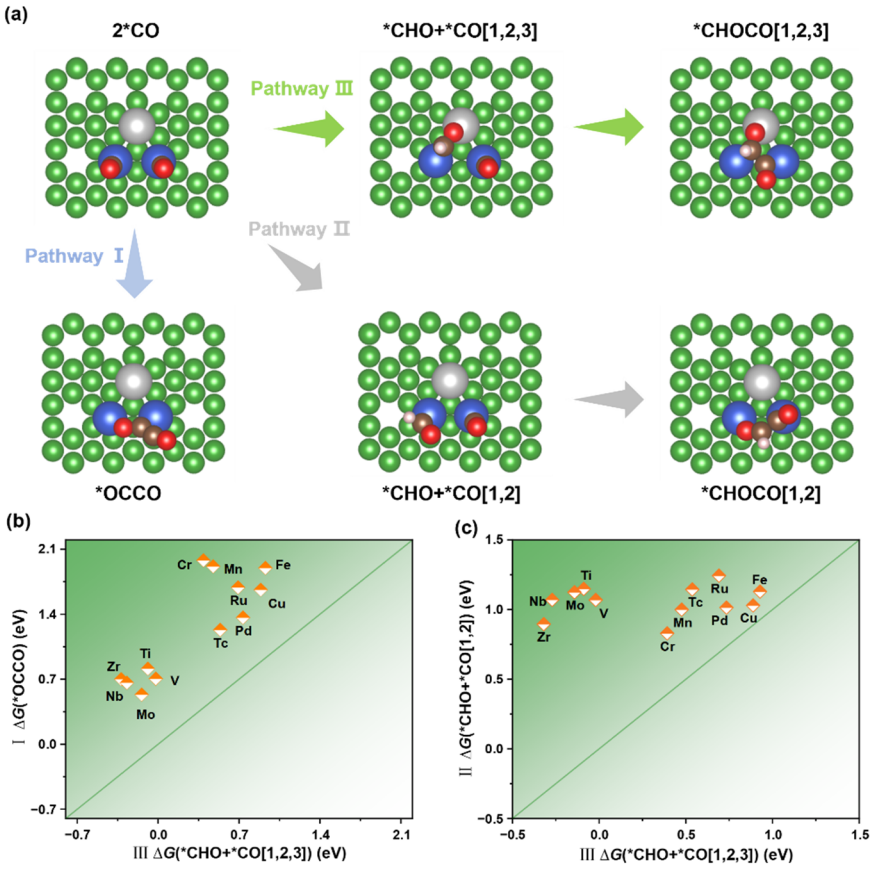


Figure 4. C–C coupling pathways on Cu_2TM/β-TBN. (**a**) Schematic of the three C–C coupling pathways. Pathway I, direct coupling of two *CO to *OCCO. Pathway II, coupling of *CHO with *CO adsorbed on a single Cu site to form *CHOCO[1,2]. Pathway III, coupling of bridge-adsorbed *CHO with *CO to form *CHOCO[1,2,3]. (**b**) Free energy comparison between *OCCO and *CHO+*CO[1,2,3]. (**c**) Free energy comparison between *CHO+*CO[1,2] and *CHO+*CO[1,2,3].

3.4. Thermodynamic-Kinetic Trade-Off in C–C Coupling

Hereafter, the notation *CHO+*CO refers specifically to the *CHO+*CO[1,2,3] configuration, and ΔG(*CHO+*CO) denotes its formation free energy. Figure 5a displays the free energy profile for pathway III, in which two *CO molecules form the *CHO+*CO precursor, and the subsequent C–C coupling to *CHOCO[1,2,3] proceeds through the transition state. Figure 5b,c present the dependence of ΔG(*CHO+*CO) and the C–C coupling transition-state energy barrier E_{TS} on ε_d(TM). Two opposing trends emerge. As ε_d(TM) shifts to lower energy from Ti through Fe, ΔG(*CHO+*CO) decreases, reflecting stronger intermediate binding. At the same time, E_{TS} increases, the coupling barrier rising as the precursor becomes more stable. Both trends are linear and hold across the fourth-period and fifth-period TM series, the latter from Zr through Tc. The direct consequence of these opposing responses to ε_d(TM) is a negative correlation between ΔG(*CHO+*CO) and E_{TS}. Overstabilizing the precursor thermodynamically exacts a kinetic penalty on the coupling step. The effective barrier E_{TS} therefore grows as ΔG(*CHO+*CO) becomes more negative. An intermediate trapped in an overly deep potential well becomes kinetically immobilized. Its strong binding raises the reorganization energy required to reach the coupling geometry to prohibitive levels. At the opposite extreme, weak binding provides insufficient stabilization to populate the precursor state. Between these limits lies a window of intermediate affinity that balances thermodynamic driving force against kinetic accessibility. Three catalysts fall within this window. Cu_2Cr/β-TBN, Cu_2Mn/β-TBN, and Cu_2Tc/β-TBN exhibit ΔG(*CHO+*CO) values that are sufficiently negative to ensure precursor coverage yet not so negative as to raise E_{TS} beyond a surmountable threshold. These three systems exemplify the principle that governs C–C coupling on this catalyst platform. The design objective is not the strongest intermediate binding but the most productive compromise between stabilization and mobility, a balance that anchors the design principle of the triatomic platform.

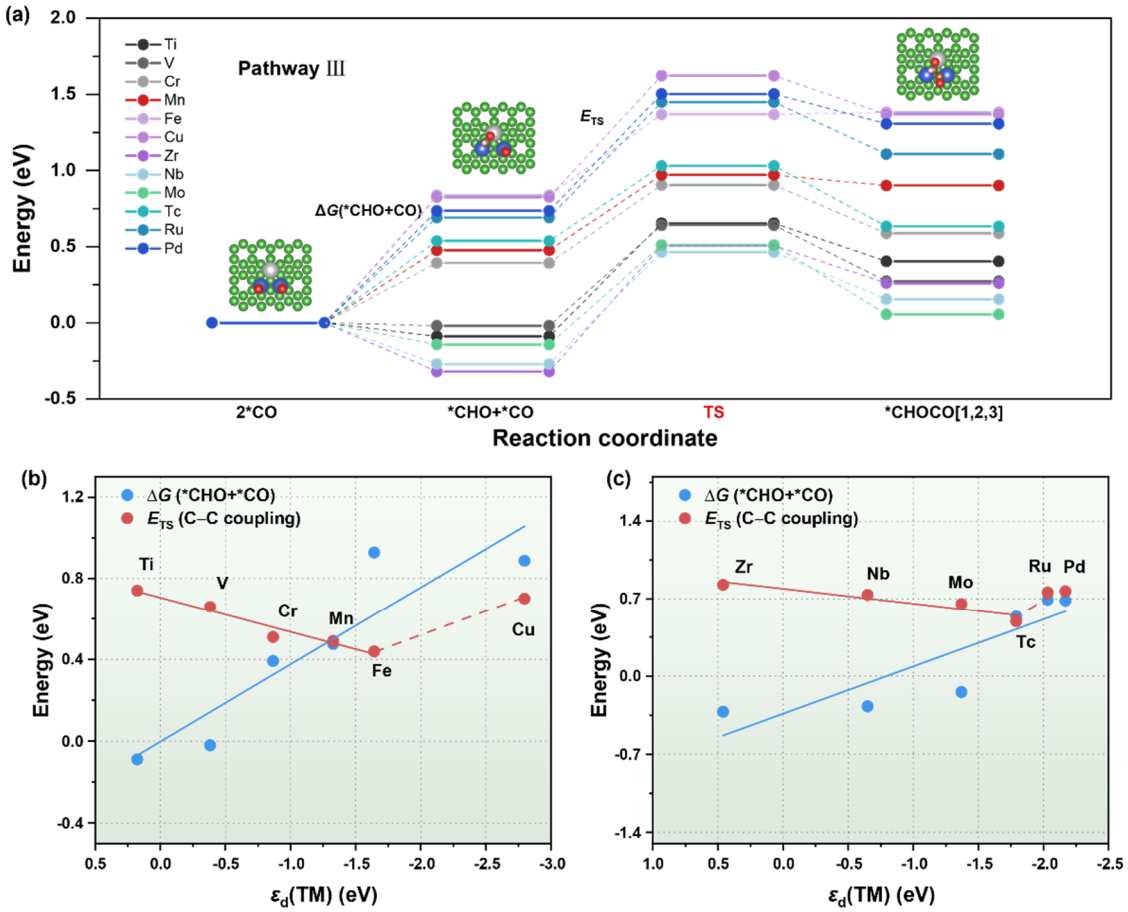


Figure 5. Thermodynamic-kinetic trade-off in C–C coupling. (**a**) Free energy profile for C–C coupling via pathway III. TS denotes the transition state. (**b**) Variation of the *CHO+*CO formation free energy, ΔG(*CHO+*CO), and the C–C coupling transition-state energy barrier, E_{TS}, as a function of ε_d(TM) for fourth-period TM dopants. (**c**) Same as (**b**) but for fifth-period TM dopants.

The thermodynamic-kinetic trade-off governing C–C coupling motivates the identification of parameters that predictively control ΔG(*CHO+*CO). Two descriptors were extracted from the electronic and geometric structure of the adsorbed *CHO+*CO intermediate (Figure 6a). The first is the Bader charge transfer ΔQ, the net electron flow between the adsorbate and the catalyst surface, with positive ΔQ indicating electron donation from the surface to the intermediate. The second is the vertical displacement of the TM atom from the β-TBN plane in the adsorbed configuration, d_L, a geometric coordinate that captures the out-of-plane relaxation of the dopant upon intermediate binding. The charge density difference map in Figure 6a visualizes this charge redistribution for a representative system.

The relative importance of these two descriptors splits sharply by period. For the fourth-period TMs (Ti, V, Cr, Mn, Fe, Cu), ΔG(*CHO+*CO) correlates strongly with ΔQ (R^2 = 0.85, Figure 6b) and substantially more weakly with d_L (R^2 = 0.35). Electron transfer is therefore the primary factor governing intermediate stability in this period, with geometric displacement playing a secondary role. For the fifth-period TMs (Zr, Nb, Mo, Tc, Ru, Pd), the hierarchy inverts. d_L now provides the dominant correlation with ΔG(*CHO+*CO) (R^2 = 0.89), while ΔQ exhibits only a weak correlation (R^2 = 0.55), as shown in Figure 6c. The vertical displacement of the larger and more polarizable fifth-period TM atoms becomes the primary geometric descriptor for intermediate free energy. ΔQ and d_L vary independently across the TM series, confirming that they capture distinct electronic and geometric degrees of freedom rather than redundant measures of the same underlying property.

This period-dependent inversion of the dominant descriptor constitutes a cross-validated separation of electronic and geometric regulatory mechanisms. For fourth-period TMs, the predictive descriptor is ΔQ. For fifth-period TMs, the predictive descriptor is d_L. Together, they form the dual-descriptor framework for rationally tuning ΔG(*CHO+*CO) and, through the thermodynamic-kinetic trade-off established above, the C–C coupling activity of Cu_2TM/β-TBN catalysts.

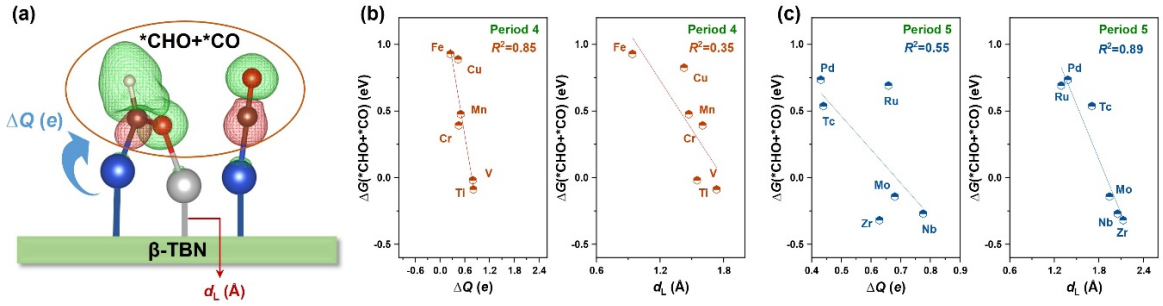


Figure 6. Electronic and geometric descriptors governing ΔG(*CHO+*CO). (**a**) Charge density difference map for the *CHO+*CO intermediate adsorbed on a representative Cu_2TM/β-TBN system. Red and green isosurfaces represent electron accumulation and depletion, respectively. ΔQ denotes the net Bader charge transfer to the adsorbate, and d_L denotes the vertical displacement of the TM atom from the β-TBN plane in the adsorbed configuration. (**b**) Left panel, linear correlation between ΔG(*CHO+*CO) and ΔQ for fourth-period TM dopants. Right panel, correlation between ΔG(*CHO+*CO) and d_L for fourth-period TM dopants. (**c**) Left panel, correlation between ΔG(*CHO+*CO) and ΔQ for fifth-period TM dopants. Right panel, linear correlation between ΔG(*CHO+*CO) and d_L for fifth-period TM dopants.

4. Conclusions

This work has addressed the question of how the electronic and geometric structure of Cu_2TM/β-TBN bimetallic triatomic clusters governs the selectivity of C–C coupling toward C_2H_4 in electrocatalytic CO_2 reduction. Through a multi-stage computational screening procedure that narrowed eighteen transition metal dopants to twelve active systems, a mechanistic picture emerges in which three factors converge. CO_2 activation occurs preferentially at the heterometallic Cu–TM bridge, its adsorption strength predictably tuned by the TM d-band center. The subsequent C–C coupling proceeds via the asymmetric coupling of bridge-adsorbed *CHO with *CO, a pathway that exploits the dual-site cooperative anchoring unique to the three-center architecture and is inaccessible on single-site or dual-site catalysts. The stability of the *CHO+*CO coupling precursor, quantified by ΔG(*CHO+*CO), competes directly with the C–C coupling transition-state energy barrier, E_{TS}. An excessively stabilized intermediate raises the kinetic barrier and impedes the coupling step. This thermodynamic-kinetic trade-off defines an optimal window of intermediate affinity, within which Cu_2Cr/β-TBN, Cu_2Mn/β-TBN, and Cu_2Tc/β-TBN emerge as promising catalysts that exemplify the balanced binding principle. Beneath these mechanistic findings lies a regulatory pattern that separates the periodic table into two distinct modes. For fourth-period transition metals, the extent of electron transfer ΔQ between the adsorbate and the surface governs

ΔG(*CHO+*CO). For fifth-period transition metals, the vertical displacement of the TM atom, d_L, assumes the dominant role, a geometric descriptor largely decoupled from charge transfer. This period-dependent inversion establishes electronic charge transfer and geometric displacement as complementary and independently variable descriptors. Together, they form a dual-descriptor framework that enables the rational tuning of intermediate stability and, through the thermodynamic-kinetic trade-off, the C–C coupling activity. These findings advance the mechanistic understanding of multisite cooperative catalysis beyond the single-site design. The dual-descriptor strategy identified here, coupling an electronic and a geometric parameter that are accessible from routine DFT calculations, provides a predictive foundation for screening and designing triatomic catalysts, and its extension to other multiatom platforms represents a productive direction for future work.

Supplementary Materials

The additional data and information can be downloaded at: https://media.sciltp.com/articles/others/26101 91614498633/NENP-26080124-SM.pdf. Figure S1. Electron localization function (ELF) maps for representative Cu_2TM/β-TBN systems. Blue corresponds to regions of low electron localization and red to regions of high electron localization. Figure S2. Schematic illustration of Cu_2TM/β-TBN with different TM dopants. Figure S3. Density of states plots of Cu_2TM/β-TBN. Figure S4. Correlation between ε_d(Cu) and ε_d(Cu_2TM) in the Cu_2TM/β-TBN structures. Figure S5. Structural illustrations of CO_2 adsorbed on Cu_2Co/β-TBN, Cu_2Ni/β-TBN, and Cu_2Ag/β-TBN. Figure S6. Distribution of ICOHP values for the TM–O bonds in *CHO+*CO adsorbed on Cu_2TM/β-TBN (TM = Ti, V, Cr, Mn, Fe, Cu, Zr, Nb, Mo, Tc, Ru, Rh, Pd, Ag). Figure S7. Proposed reaction pathways for the conversion of CO_2 to C_2H_4 via electrocatalytic reduction on Cu_2TM/β-TBN. Figure S8. Free energy diagrams for the electrocatalytic reduction of 2*CO to C_2H_4 on Cu_2TM/β-TBN (TM = Ti, V, Cr, Mn, Fe, Cu). Figure S9. Free energy diagrams for the electrocatalytic reduction of 2*CO to C_2H_4 on Cu_2TM/β-TBN (TM = Zr, Nb, Mo, Tc, Ru, Pd). Table S1. Summary of interatomic distances $d_{Cu(1)–Cu(2)}$, $d_{Cu(1)–TM}$, and $d_{Cu(2)–TM}$, vertical displacement $d_{TM–β-TBN}$, and binding energies E_b of Cu_2TM/β-TBN. Table S2. Adsorption energies of $*CO_2$ in three different configurations on Cu_2TM/β-TBN. Table S3. Magnetic moments of bare clusters and intermediate states.

Author Contributions

S.W.: data curation, formal analysis, investigation, software, validation, visualization, writing—original draft, writing—review & editing; H.W.: formal analysis, investigation, software, validation, visualization, writing—original draft; P.B.: formal analysis, investigation, software, validation, visualization; L.X.: conceptualization, funding acquisition, methodology, project administration, resources, supervision, writing—original draft, writing—review & editing. All authors have read and agreed to the published version of the manuscript.

Funding

This study was funded by the Scientific Research Innovation Capability Support Project for Young Faculty (ZYGXQNJSKYCXNLZCXM-E16) and the Fundamental and Interdisciplinary Disciplines Breakthrough Plan of the Ministry of Education of China (JYB2025XDXM308).

Institutional Review Board Statement

Not applicable.

Informed Consent Statement

Not applicable.

Data Availability Statement

The data that support the findings of this study are available from the corresponding author upon reasonable request.

Conflicts of Interest

The authors declare no conflict of interest.

Use of AI and AI-Assisted Technologies

No AI tools were utilized for this paper.

Symbols

β-TBN	β-phase tetragonal borophene
Cu_2TM	Triatomic cluster composed of two Cu atoms and one TM atom
Cu(1)	Cu atom labeled as site 1
Cu(2)	Cu atom labeled as site 2
TM	Transition metal atom
$d_{Cu(1)–Cu(2)}$	Interatomic distance between Cu(1) and Cu(2)
$d_{Cu(1)–TM}$	Interatomic distance between Cu(1) and TM
$d_{Cu(2)–TM}$	Interatomic distance between Cu(2) and TM
$d_{TM–β-TBN}$	Vertical displacement of the TM atom from the β-TBN plane in the absence of any adsorbates
ε_d(TM)	d-band center of TM
ε_d(Cu)	d-band center of Cu
$\varepsilon_d(Cu_2TM)$	d-band center of Cu_2TM cluster
O(1)	Oxygen atom of adsorbed CO_2 that is not coordinated to any cluster atom
O(2)	Oxygen atom of adsorbed CO_2 that is bound to the TM site
$d_{C–O(1)}$	Bond length between C and O(1)
$d_{C–O(2)}$	Bond length between C and O(2)
θ	O–C–O bond angle of adsorbed CO_2
E_b	Binding energy
E_{ads}	Adsorption energy
ΔG	Gibbs free energy change
E_{TS}	Transition-state energy barrier for C–C coupling
R^2	Coefficient of determination
$d_{TM–O}$	TM–O bond in the adsorbed species
*CO_2	Adsorbed CO_2 species
*CO	Adsorbed CO species
*CHO	Adsorbed CHO species
*CHOCO	Coupled product of *CHO and *CO
*CHO+*CO	Coexisting *CHO and *CO intermediates as two independent adsorbates
d_L	Vertical displacement of the TM atom from the β-TBN plane in the *CHO+*CO adsorbed configuration
ΔQ	Bader charge transfer between the adsorbate and the catalyst surface

References

1. Yin, Z.; Sun, H.; Li, W.; et al. Rational Design of Photocatalysts for CO_2 Reduction to Multi-Carbon Products. *Nano-Electrochem. Nano-Photochem.* **2025**, *1*, 6. https://doi.org/10.53941/nenp.2025.100006.
2. Zhu, W. Living Bioreactive Facades for Visible Carbon Reduction in Cities. *Nat. Cities* **2026**, *3*, 784–785. https://doi.org/10.1038/s44284-026-00502-3.
3. Wei, S.; Liu, W.; Xu, L. Unified Effects of Lanthanoid Elements and Magnetic Fields on the Electrocatalytic CO_2 Reduction Reaction. *J. Mater. Chem. A* **2026**, *14*, 23684–23697. https://doi.org/10.1039/d6ta01120a.
4. Liu, J.; Burciaga, R.; Tang, S.; et al. Heterogeneous Catalysis for the Environment. *Innov. Mater.* **2024**, *2*, 100090. https://doi.org/10.59717/j.xinn-mater.2024.100090.
5. Li, P.; Yang, R.; Zhu, W. Quantum-Dot-Based Catalysts for Electrochemical CO_2 Reduction: Structure–Selectivity Relationships and Design Principles. *J. Electroanal. Chem.* **2026**, *1015*, 120234. https://doi.org/10.1016/j.jelechem.2026.120234.
6. Liu, W.; Bai, P.; Wei, S.; et al. Electron-Rich Cu^0-Cu_2O Heterogeneous Interface Constructed via Controllable Electrochemical Reconstruction for a Single CO_2 Deep-Reduction Product Ethylene. *Appl. Catal. B Environ. Energy* **2024**, *348*, 123831. https://doi.org/10.1016/j.apcatb.2024.123831.
7. Xie, L.; Liu, Y.; Li, S.; et al. Phase and Facet Engineering for Nanoscale Catalyst Discovery in Electrochemical CO_2 Reduction. *Nat. Synth.* **2026**, *5*, 489–505. https://doi.org/10.1038/s44160-026-01025-4.
8. Li, H.; Zhou, H.; Zhou, Y.; et al. Electric-Field Promoted C–C Coupling over Cu Nanoneedles for CO_2 Electroreduction to C_2 Products. *Chin. J. Catal.* **2022**, *43*, 519–525. https://doi.org/10.1016/s1872-2067(21)63866-4.
9. Kim, Y.; Park, S.; Shin, S.J.; et al. Time-Resolved Observation of C–C Coupling Intermediates on Cu Electrodes for Selective Electrochemical CO_2 Reduction. *Energy Environ. Sci.* **2020**, *13*, 4301–4311. https://doi.org/10.1039/d0ee01690j.
10. Li, L.; Li, X.; Sun, Y.; et al. Rational Design of Electrocatalytic Carbon Dioxide Reduction for a Zero-Carbon Network.

Chem. Soc. Rev. **2022**, *51*, 1234–1252. https://doi.org/10.1039/d1cs00893e.
11. Xu, D.; Li, K.; Jia, B.; et al. Electrocatalytic CO_2 Reduction towards Industrial Applications. *Carbon Energy* **2023**, *5*, e230. https://doi.org/10.1002/cey2.230.
12. Zhu, L.; Liu, K.; Huang, J.L.; et al. Plasmon-Enhanced C_2H_4 Generation in the CO_2 Electroreduction Reaction on a CuPd Tandem Catalyst. *J. Am. Chem. Soc.* **2025**, *147*, 33003–33009. https://doi.org/10.1021/jacs.5c10517.
13. Wang, H.; Liu, W.; Xu, S.; et al. Molecular Interface Directs Asymmetric C–C Coupling toward Durable, Selective, and High-Rate Ethylene Electrosynthesis from CO_2. *Appl. Catal. B Environ. Energy* **2027**, *400*, 127232. https://doi.org/10.1016/j.apcatb.2026.127232.
14. Chen, C.; Yu, S.; Yang, Y.; et al. Exploration of the Bio-Analogous Asymmetric C–C Coupling Mechanism in Tandem CO_2 Electroreduction. *Nat. Catal.* **2022**, *5*, 878–887. https://doi.org/10.1038/s41929-022-00844-w.
15. Zhang, B.; Zhang, B.; Jiang, Y.; et al. Single-Atom Electrocatalysts for Multi-Electron Reduction of CO_2. *Small* **2021**, *17*, 2101443. https://doi.org/10.1002/smll.202101443.
16. Min, J.; Liu, L.; Chen, F.; et al. Theoretical Exploration on the Activity of Copper Single-Atom Catalysts for Electrocatalytic Reduction of CO_2. *J. Mater. Chem. A* **2023**, *11*, 7735–7745. https://doi.org/10.1039/d2ta09599h.
17. Zhang, Y.; Zhao, J.; Lin, S. Nitrogen Doping Retrofits the Coordination Environment of Copper Single-Atom Catalysts for Deep CO_2 Reduction. *Chin. J. Struct. Chem.* **2024**, *43*, 100415. https://doi.org/10.1016/j.cjsc.2024.100415.
18. Zhang, F.; Gong, L.; Liu, M.; et al. Nature of C–C Coupling and Strategy of Tuning the Catalytic Activity of Cu-N-C Catalysts for Electro-Reduction of CO_2 to Ethanol. *Nano Energy* **2024**, *127*, 109699. https://doi.org/10.1016/j.nanoen.2024.109699.
19. Wang, H.; Liu, W.; Xu, S.; et al. Regulation of Ni Single-Atom/Nanoparticle Cooperative Catalytic Systems by P Heteroatom Asymmetric Coordination for Efficient Electrocatalytic CO_2 Reduction. *Small* **2025**, *21*, 2504251. https://doi.org/10.1002/smll.202504251.
20. Chen, Y.; Lin, J.; Pan, Q.; et al. Inter-Metal Interaction of Dual-Atom Catalysts in Heterogeneous Catalysis. *Angew. Chem. Int. Ed.* **2023**, *62*, e202306469. https://doi.org/10.1002/anie.202306469.
21. Liu, W.; Wang, H.; Xu, S.; et al. A Cu–La Dual-Atomic Catalyst with Dual-Site Adsorption Enables Synergistic Optimization of Thermodynamics and Kinetics of Electrocatalytic CO_2 Reduction. *Angew. Chem. Int. Ed.* **2026**, *65*, e21626. https://doi.org/10.1002/anie.202521626.
22. Bai, S.; He, Z.; Zheng, W.; et al. Heteroatom-Engineered Triatomic Cu Cluster on g-C_3N_4 for Selective CO_2-to-Ethylene Electrocatalysis. *Adv. Mater.* **2026**, *38*, e73318. https://doi.org/10.1002/adma.73318.
23. Chen, Z.W.; Chen, L.X.; Yang, C.C.; et al. Atomic (Single, Double, and Triple Atoms) Catalysis: Frontiers, Opportunities, and Challenges. *J. Mater. Chem. A* **2019**, *7*, 3492–3515. https://doi.org/10.1039/c8ta11416a.
24. Pan, Y.; Li, H.; Xiong, J.; et al. Protecting the State of Cu Clusters and Nanoconfinement Engineering over Hollow Mesoporous Carbon Spheres for Electrocatalytical C–C Coupling. *Appl. Catal. B Environ.* **2022**, *306*, 121111. https://doi.org/10.1016/j.apcatb.2022.121111.
25. Mannix, A.J.; Zhou, X.F.; Kiraly, B.; et al. Synthesis of Borophenes: Anisotropic, Two-Dimensional Boron Polymorphs. *Science* **2015**, *350*, 1513–1516. https://doi.org/10.1126/science.aad1080.
26. Feng, B.; Zhang, J.; Zhong, Q.; et al. Experimental Realization of Two-Dimensional Boron Sheets. *Nat. Chem.* **2016**, *8*, 563–568. https://doi.org/10.1038/nchem.2491.
27. Abdi, Y.; Mazaheri, A.; Hajibaba, S.; et al. A Two-Dimensional Borophene Supercapacitor. *ACS Mater. Lett.* **2022**, *4*, 1929–1936. https://doi.org/10.1021/acsmaterialslett.2c00475.
28. Liu, M.; Rao, F.; Xu, T.; et al. Reaction Mechanism of Metal-Free Borophene Catalyst Electrochemical Reduction of CO_2. *Colloids Surf. A Physicochem. Eng. Asp.* **2024**, *701*, 134933. https://doi.org/10.1016/j.colsurfa.2024.134933.
29. Liu, M.; Balamurugan, J.; Liang, T.; et al. Mechanism of Electrocatalytic CO_2 Reduction Reaction by Borophene Supported Bimetallic Catalysts. *J. Colloid Interface Sci.* **2024**, *659*, 959–973. https://doi.org/10.1016/j.jcis.2024.01.051.
30. Wang, Z.Q.; Lü, T.Y.; Wang, H.Q.; et al. Review of Borophene and Its Potential Applications. *Front. Phys.* **2019**, *14*, 33403. https://doi.org/10.1007/s11467-019-0884-5.
31. Liu, L.; Yang, L.; Zhang, H.; et al. Screening Strategies for Diatom Metal-Doped β-Borophene Nanosheet Catalysts for Electrochemical Synthesis of Ammonia Using Density Functional Theory. *Energy Fuels* **2023**, *37*, 9682–9691. https://doi.org/10.1021/acs.energyfuels.3c01231.
32. Kresse, G.; Hafner, J. Ab Initio Molecular Dynamics for Liquid Metals. *Phys. Rev. B* **1993**, *47*, 558–561. https://doi.org/10.1103/physrevb.47.558.
33. Kresse, G.; Hafner, J. Ab Initio Molecular-Dynamics Simulation of the Liquid-Metal–Amorphous-Semiconductor Transition in Germanium. *Phys. Rev. B* **1994**, *49*, 14251–14269. https://doi.org/10.1103/physrevb.49.14251.
34. Kresse, G.; Furthmüller, J. Efficiency of Ab-Initio Total Energy Calculations for Metals and Semiconductors Using a Plane-Wave Basis Set. *Comput. Mater. Sci.* **1996**, *6*, 15–50. https://doi.org/10.1016/0927-0256(96)00008-0.
35. Kresse, G.; Furthmüller, J. Efficient Iterative Schemes for Ab Initio Total-Energy Calculations Using a Plane-Wave Basis Set. *Phys. Rev. B* **1996**, *54*, 11169–11186. https://doi.org/10.1103/physrevb.54.11169.

36. Blöchl, P.E. Projector Augmented-Wave Method. *Phys. Rev. B* **1994**, *50*, 17953–17979. https://doi.org/10.1103/physrevb.50.17953.
37. Kresse, G.; Joubert, D. From Ultrasoft Pseudopotentials to the Projector Augmented-Wave Method. *Phys. Rev. B* **1999**, *59*, 1758–1775. https://doi.org/10.1103/physrevb.59.1758.
38. Perdew, J.P.; Burke, K.; Ernzerhof, M. Generalized Gradient Approximation Made Simple. *Phys. Rev. Lett.* **1996**, *77*, 3865–3868. https://doi.org/10.1103/physrevlett.77.3865.
39. Monkhorst, H.J.; Pack, J.D. Special Points for Brillouin-Zone Integrations. *Phys. Rev. B* **1976**, *13*, 5188–5192. https://doi.org/10.1103/physrevb.13.5188.
40. Grimme, S.; Antony, J.; Ehrlich, S.; et al. A Consistent and Accurate Ab Initio Parametrization of Density Functional Dispersion Correction (DFT-D) for the 94 Elements H-Pu. *J. Chem. Phys.* **2010**, *132*, 154104. https://doi.org/10.1063/1.3382344.
41. Nørskov, J.K.; Rossmeisl, J.; Logadottir, A.; et al. Origin of the Overpotential for Oxygen Reduction at a Fuel-Cell Cathode. *J. Phys. Chem. B* **2004**, *108*, 17886–17892. https://doi.org/10.1021/jp047349j.
42. Dronskowski, R.; Bloechl, P.E. Crystal Orbital Hamilton Populations (COHP): Energy-Resolved Visualization of Chemical Bonding in Solids Based on Density-Functional Calculations. *J. Phys. Chem.* **1993**, *97*, 8617–8624. https://doi.org/10.1021/j100135a014.
43. Deringer, V.L.; Tchougréeff, A.L.; Dronskowski, R. Crystal Orbital Hamilton Population (COHP) Analysis as Projected from Plane-Wave Basis Sets. *J. Phys. Chem. A* **2011**, *115*, 5461–5466. https://doi.org/10.1021/jp202489s.
44. Maintz, S.; Deringer, V.L.; Tchougréeff, A.L.; et al. LOBSTER: A Tool to Extract Chemical Bonding from Plane-Wave Based DFT. *J. Comput. Chem.* **2016**, *37*, 1030–1035. https://doi.org/10.1002/jcc.24300.
45. Nelson, R.; Ertural, C.; George, J.; et al. LOBSTER: Local Orbital Projections, Atomic Charges, and Chemical-Bonding Analysis from Projector-Augmented-Wave-Based Density-Functional Theory. *J. Comput. Chem.* **2020**, *41*, 1931–1940. https://doi.org/10.1002/jcc.26353.
46. Henkelman, G.; Uberuaga, B.P.; Jónsson, H. A Climbing Image Nudged Elastic Band Method for Finding Saddle Points and Minimum Energy Paths. *J. Chem. Phys.* **2000**, *113*, 9901–9904. https://doi.org/10.1063/1.1329672.
47. Li, C.F.; Guo, R.T.; Zhang, Z.R.; et al. Converting CO_2 into Value-Added Products by Cu_2O-Based Catalysts: From Photocatalysis, Electrocatalysis to Photoelectrocatalysis. *Small* **2023**, *19*, 2207875. https://doi.org/10.1002/smll.202207875.
48. Cui, H.F.; Yang, F.; Liu, C.; et al. Recent Progress of Covalent Organic Frameworks-Based Materials Used for CO_2 Electrocatalytic Reduction: A Review. *Small* **2025**, *21*, 2502867. https://doi.org/10.1002/smll.202502867.